

BSGS: Bi-stage 3D Gaussian Splatting for Camera Motion Deblurring

An Zhao

Nanjing University of Aeronautics and Astronautics
Nanjing, China
anzhao@nuaa.edu.cn

Zhe Zhu

Nanjing University of Aeronautics and Astronautics
Nanjing, China
zhuzhe0619@nuaa.edu.cn

Piaopiao Yu*

Nanjing University of Aeronautics and Astronautics
Nanjing, China
yupiaopiao@nuaa.edu.cn

Mingqiang Wei*

Nanjing University of Aeronautics and Astronautics
Nanjing, China
mqwei@nuaa.edu.cn

Abstract

3D Gaussian Splatting has exhibited remarkable capabilities in 3D scene reconstruction. However, reconstructing high-quality 3D scenes from motion-blurred images caused by camera motion poses a significant challenge.

The performance of existing 3DGS-based deblurring methods are limited due to their inherent mechanisms, such as extreme dependence on the accuracy of camera poses and inability to effectively control erroneous Gaussian primitives densification caused by motion blur. To solve these problems, we introduce a novel framework, Bi-Stage 3D Gaussian Splatting, to accurately reconstruct 3D scenes from motion-blurred images. BSGS contains two stages. First, Camera Pose Refinement roughly optimizes camera poses to reduce motion-induced distortions. Second, with fixed rough camera poses, Global Rigid Transformation further corrects motion-induced blur distortions. To alleviate multi-subframe gradient conflicts, we propose a subframe gradient aggregation strategy to optimize both stages. Furthermore, a space-time bi-stage optimization strategy is introduced to dynamically adjust primitive densification thresholds and prevent premature noisy Gaussian generation in blurred regions. Comprehensive experiments verify the effectiveness of our proposed deblurring method and show its superiority over the state of the arts.

CCS Concepts

• **Computing methodologies** → *3D Reconstruction*.

Keywords

Camera Motion-blurred Images, 3D Gaussian Splatting, Rigid Transformation, Subframe Gradient Aggregation, Space-time Bi-stage Optimization

*Corresponding Author

Permission to make digital or hard copies of all or part of this work for personal or classroom use is granted without fee provided that copies are not made or distributed for profit or commercial advantage and that copies bear this notice and the full citation on the first page. Copyrights for components of this work owned by others than the author(s) must be honored. Abstracting with credit is permitted. To copy otherwise, or republish, to post on servers or to redistribute to lists, requires prior specific permission and/or a fee. Request permissions from permissions@acm.org.

MM '25, October 27–31, 2025, Dublin, Ireland

© 2025 Copyright held by the owner/author(s). Publication rights licensed to ACM.
ACM ISBN 979-8-4007-2035-2/2025/10
<https://doi.org/10.1145/3746027.3755449>

ACM Reference Format:

An Zhao, Piaopiao Yu, Zhe Zhu, and Mingqiang Wei. 2025. BSGS: Bi-stage 3D Gaussian Splatting for Camera Motion Deblurring. In *Proceedings of the 33rd ACM International Conference on Multimedia (MM '25)*, October 27–31, 2025, Dublin, Ireland. ACM, New York, NY, USA, 9 pages. <https://doi.org/10.1145/3746027.3755449>

1 INTRODUCTION

Reconstructing a 3D scene from 2D images stands as a core issue in computer vision. Among various pioneering approaches, Neural Radiance Fields (NeRF) [22] has emerged as a prominent solution, demonstrating remarkable performance in recovering high-fidelity 3D scenes through its innovative differentiable volume rendering. Meanwhile, 3D Gaussian Splatting (3DGS) [10] represents 3D scenes through Gaussian points and enables real-time rendering through efficient rasterization while preserving visual quality. However, both NeRF-based and 3DGS-based methods heavily depend on high-quality input images. In real-world scenarios, captured images are often affected by camera motion blur, which inevitably degrades reconstruction quality. Camera motion blur is a prevalent form of image degradation, typically arising from camera jitter during exposure. Images affected by camera motion blur exhibit significant geometric inconsistencies between multi-view frames. Compounding this problem, the camera poses recovered from motion-blurred images using COLMAP [34] are often significantly biased, causing geometric misalignment when utilizing NeRF [22] and 3DGS [10] for reconstruction. Furthermore, the sparse point clouds reconstructed from blurred images tend to contain substantial noise, severely affecting the quality of 3DGS initialization and resulting in marked degradation of performance.

Recently, several nerf-based approaches [13, 14, 16, 29, 39] have emerged to process motion-blurred images to accurately reconstruct 3D scenes. Deblur-NeRF [21] and DP-NeRF [13] attempt to model blur kernels and integrate physical priors, suffering from computationally intensive optimization processes. BAD-NeRF [39] and ExBluRF [14] jointly optimize camera poses and NeRF parameters, yet constrained by NeRF's inherent limitations, including low training efficiency. 3DGS-based methods [2, 12, 15, 24, 30, 47] have also incorporated motion blur modeling into their frameworks. BAD-GS [47] uses spline functions to represent camera trajectories during exposure time. DeBlur-GS [2] derives camera pose derivatives to simplify the estimation of camera poses. However, existing

methods often overlook that motion blur-induced errors in sparse point cloud initialization frequently cause premature and erroneous Gaussian splitting during training. In addition, their exclusive focus on camera pose optimization leads to excessive computational demands and heightened overfitting risks. More critically, these methods are extremely sensitive to pose estimation accuracy where even minimal deviations can lead to severe degradation in reconstruction quality.

To address these challenges, we propose Bi-Stage 3D Gaussian Splatting (BSGS), a framework for robust 3D reconstruction from motion-blurred images. BSGS includes two main steps: Camera Pose Refinement, which estimates approximate camera poses, and Global Rigid Transformation, where we apply global transformations to Gaussian points using the refined poses. In these two stages, we use weighted blending on subframes to mitigate gradient conflicts.

BSGS can effectively correct motion-induced distortions and reduce sensitivity to precise pose estimation. For scene optimization, we minimize the photometric error between input blurred images and virtual synthesized images, supplemented by a max-pooling-based subframe gradient aggregation strategy to resolve multi-frame gradient conflicts. To further mitigate sparse point cloud initialization errors, we introduce Space-Time Coupled Den-sification. This adaptive thresholding mechanism adjusts Gaussian densification parameters dynamically, preventing premature artifact generation in blurred regions, outperforming fixed-threshold methods which previously methods used.

Our experimental results show that our BSGS effectively handles motion-blurred images, enabling the synthesis of sharp results in novel views. In summary, our main contributions are three-fold:

- We introduce a two-stage training framework: Camera Pose Refinement to estimate camera poses; Global Rigid Transformation to simulate camera blur generation and correct motion-induced blur distortions.
- We develop a subframe gradient aggregation strategy to alleviate the gradient direction conflicts.
- We propose Space-Time Coupling Den-sification to prevent noise propagation and optimize Gaussian distribution.

2 RELATED WORK

2.1 Novel View Synthesis

The emergence of Neural Radiance Fields (NeRF) [22] has significantly advanced the field of 3D vision, particularly in the context of novel view synthesis from multi-view images. However, in NeRF, the MLP layers required to evaluate the density and color at each pixel are computationally expensive, leading to slow rendering times. This has motivated further research into methods to accelerate both training and rendering processes [1, 6, 45]. The advent of 3D Gaussian Splatting (3DGS) [10] has significantly addressed this issue by introducing an explicit point-based representation and a novel differentiable splatting rasterizer, enabling real-time rendering without compromising visual quality. Subsequent works have extended NeRF and 3DGS to various domains, including dynamic 3D scene reconstruction [17, 18, 26, 27, 32, 38], human and facial reconstruction [7, 9, 31, 40], and 3D content generation [3, 19, 20, 25, 33, 36, 41, 43, 44, 48].

Despite the impressive advancements achieved by NeRF and 3DGS, most of these methods still rely on accurate camera parameters and sharp images, and struggle to effectively handle blurry input images. Our method addresses this challenge by incorporating camera motion blur deblurring into the 3D Gaussian Splatting framework, leveraging explicit point-based representations to recover sharp, high-quality scenes from blurry inputs while enabling real-time rendering of the reconstructed scenes.

2.2 2D Image Deblurring

Image deblurring is a fundamental problem in the field of image restoration, primarily addressing degradation caused by camera motion, defocus, or object movement during image acquisition.

Deep learning-based CNN methods [11, 23, 35, 37] learn end-to-end mappings but require large datasets and generalize poorly. Multi-scale approaches [8, 37, 46] improve detail recovery but ignore 3D geometry, harming multi-view consistency.

In contrast to the aforementioned 2D deblurring methods, our approach does not rely on a pre-trained network trained on large-scale datasets. Instead, we take advantage of multi-view consistency and employ a differentiable splatting rasterizer with a 3D Gaussian representation. This allows for high-quality 3D scene reconstruction and significantly improves the accuracy and robustness of the deblurring process.

2.3 Radiance Field Deblurring

Recently, deblurring methods [2, 13, 14, 21, 24, 30, 39] based on NeRF and 3DGS have made significant progress in deblurring tasks. Deblur-NeRF [21] embeds blind deblurring into NeRF, while DP-NeRF [13] models rigid blur kernels via 3D camera motion. BAD-NeRF [39], BAD-GS [47] and Deblur-GS [24] adopt physical modeling of camera motion and interpolate between predicted initial and final camera poses to optimize camera poses and scene representation parameters. Lee et al. [12] attributed the blur to the covariances of Gaussian points and proposed an MLP-based approach that predicts offsets for rotation and scale, effectively alleviating pixel-level blur effects. However, their method is limited to addressing defocus blur and does not account for motion-related blur.

3 METHOD

Given a sequence of motion-blurred images, our goal is to recover a sharp 3D scene representation. As shown in Fig. 1, our approach employs a bi-stage framework (BSGS) to deal with motion-blurred images, including Camera Pose Refinement and Global Rigid Transformation. While the former optimizes the camera poses to achieve an approximate estimate, the latter then applies global rigid transformations to the Gaussian points and simulates the camera motion blur generation with fixed camera poses. Furthermore, we propose the gradient aggregation strategy and the space-time coupling densification strategy to improve our scene reconstruction quality. The details of each content will be presented in the following sections.

3.1 Motion-Blurred Image Formation

Motion blur in digital imaging arises from camera movement during the exposure period. The motion-blurred image B is expressed as

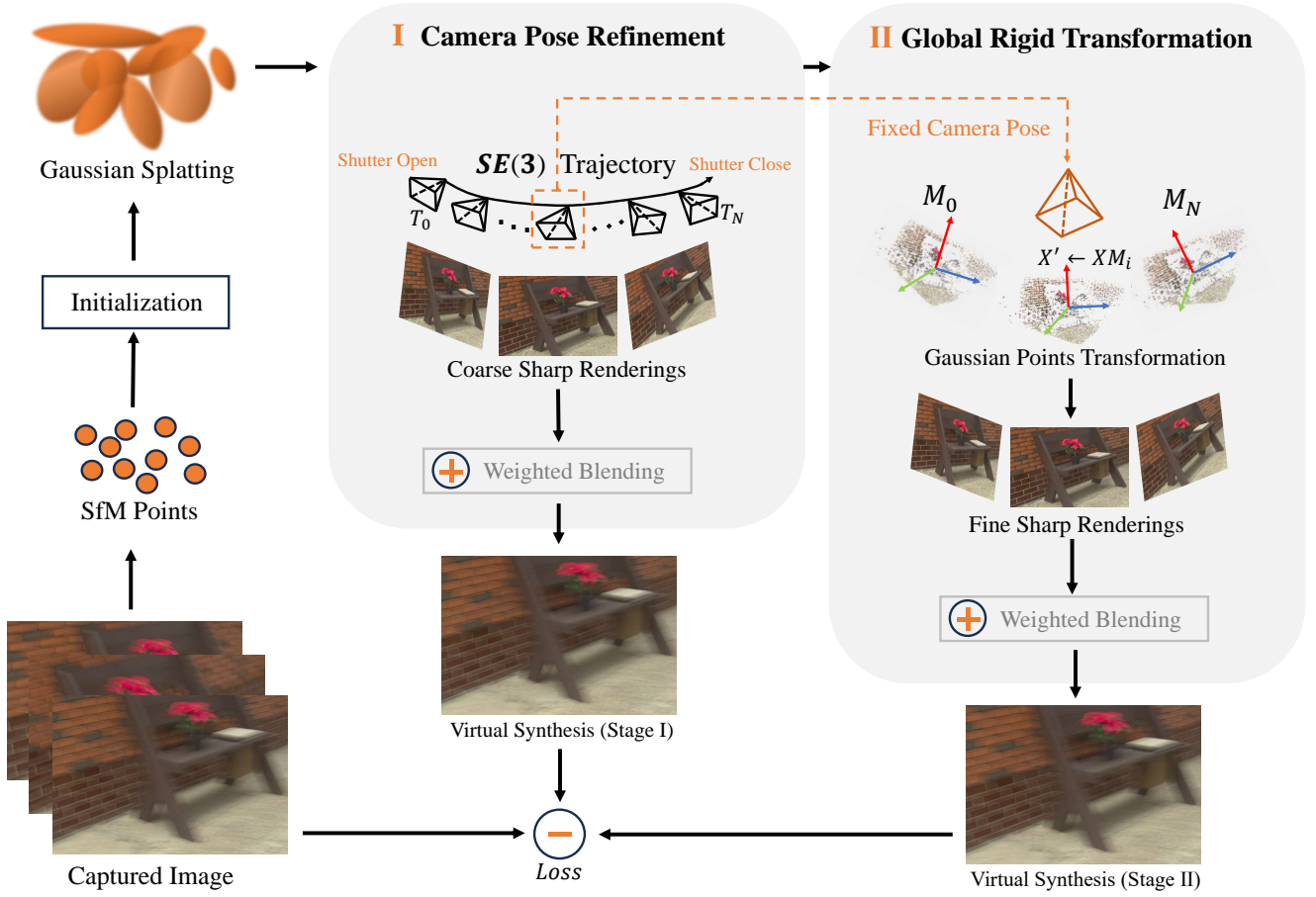


Figure 1: The pipeline of our method. We propose a Bi-stage approach for robust 3D reconstruction from motion-blurred images. In the first stage, we refine the camera poses to obtain an approximate estimate. In the second stage, we fix the optimized camera poses and apply global rigid transformations to the Gaussian points, simulating the motion blur. We optimize the Gaussian scene by minimizing photometric errors and introduce a subframe gradient aggregation strategy to resolve conflicts.

an integral of sharp images across the exposure duration τ :

$$\hat{\mathbf{B}} = \phi \int_0^\tau C_t dt, \quad (1)$$

where ϕ is a normalization factor, and C_t represents the virtual latent sharp image captured at time $t \in [0, \tau]$ within the exposure. Eq. 1 captures the cumulative effect of light integration by the camera’s photosensitive elements as the camera moves during exposure.

The extent of motion blur is intrinsically related to both the camera’s velocity and the duration of exposure. Fast camera movements or short exposure usually result in an extremely low degree of blurring, while slow movements or long exposure times will increase the degree of blurring due to the increased relative motion amplitude. In practice, the motion-blurred image can be computed as a weighted sum of sharp images sampled at discrete timestamps:

$$\hat{\mathbf{B}} \approx \sum_{i=0}^{n-1} w_i \cdot C_i. \quad (2)$$

Here, w_i denotes the weight associated with each sharp image C_i acquired at discrete time t_i . Our approach sets w_i as a learnable parameter for optimizing the compositing effect of virtual sharp images. This physical model is fundamental for our work.

3.2 Bi-Stage Deblurring Framework

We parameterize the camera pose as $T \in \text{SE}(3)$ and employ three distinct interpolation schemes (linear, cubic spline, and Bézier) to model the camera’s motion trajectory during the exposure interval. Given the initial camera pose T_{start} and the terminal pose T_{end} within the exposure period, the virtual camera pose at any intermediate timestamp $t \in [0, \tau]$ can be formulated as:

$$T_t = T_{\text{start}} \cdot \exp\left(\frac{t}{\tau} \log(T_{\text{start}}^{-1} \cdot T_{\text{end}})\right). \quad (3)$$

As shown in Fig. 1, given N motion-blurred images $\{\mathbf{B}_j\}_{j=1}^N$ and their corresponding inaccurate camera poses, we estimate a dedicated camera trajectory for each image B_j to model its specific motion characteristics during exposure. Following Eq. 2, we render

a sequence of images along the estimated camera trajectory through rasterization, which are then fused into a virtual synthesized image \hat{B} via weighted blending with learnable parameters. Our 3D scene is optimized by minimizing the loss function as:

$$\mathcal{L} = (1 - \lambda)\mathcal{L}_1 + \lambda\mathcal{L}_{D-SSIM}. \quad (4)$$

3.2.1 Camera Pose Refinement. To optimize the Gaussian parameters θ and the camera poses T (i.e., T_{start} and T_{end}) for each image, we compute the gradient of the loss function \mathcal{L} with respect to the camera poses. This gradient is expressed as:

$$\frac{\partial \mathcal{L}}{\partial T} = \sum_{j=0}^{N-1} \frac{\partial \mathcal{L}}{\partial \hat{B}_j} \cdot \frac{1}{n} \sum_{i=0}^{n-1} \frac{\partial \hat{B}_j}{\partial C_i} \left(\frac{\partial C_i}{\partial c_i} \cdot \frac{\partial c_i}{\partial T} + \frac{\partial C_i}{\partial \alpha_i} \cdot \frac{\partial \alpha_i}{\partial T} \right), \quad (5)$$

$$\frac{\partial \alpha_i}{\partial T} = \frac{\partial \alpha_i}{\partial o_i} \cdot \frac{\partial o_i}{\partial T} + \frac{\partial \alpha_i}{\partial \Sigma'_i} \cdot \frac{\partial \Sigma'_i}{\partial T} + \frac{\partial \alpha_i}{\partial \mu'_i} \cdot \frac{\partial \mu'_i}{\partial T} \quad (6)$$

where \hat{B}_j represents the virtual synthesized blurred images and C_i the corresponding rendered pixel color.

Because the color term c_i and the opacity term o_i are independent of the camera pose, the two parameters can thus be ignored in the optimization process. Due to superabundant matrix derivatives and transposition, the computational cost of calculating $\frac{\partial \Sigma'_i}{\partial T}$ is prohibitively high [42]. To alleviate it, we ignore covariance when optimizing camera poses. Because the Gaussian enter has a much larger impact on the camera pose optimization than the covariance, ignoring the covariance has negligible impact on the camera pose optimization. Finally, our gradient formula is expressed as:

$$\frac{\partial \mathcal{L}}{\partial T} = \sum_{j=0}^{N-1} \frac{\partial \mathcal{L}}{\partial \hat{B}_j} \cdot \frac{1}{n} \sum_{i=0}^{n-1} \frac{\partial \hat{B}_j}{\partial C_i} \cdot \frac{\partial C_i}{\partial \alpha_i} \cdot \frac{\partial \alpha_i}{\partial \mu_i} \cdot \frac{\partial \mu_i}{\partial \mu'_i} \cdot \frac{\partial \mu'_i}{\partial T}. \quad (7)$$

where $\mu'_i = R\mu_i + t$, representing the transformation of the i -th Gaussian's center μ_i from world coordinates to camera coordinates, with $R \in SO(3)$ denoting the rotation matrix and $t \in \mathbb{R}^3$ the translation vector of the camera pose T . During optimization, the camera pose T is iteratively adjusted to minimize the photometric discrepancy between virtual synthesized blurred images \hat{B}_j and the input blurry images B_j , thereby refining the estimated camera trajectory.

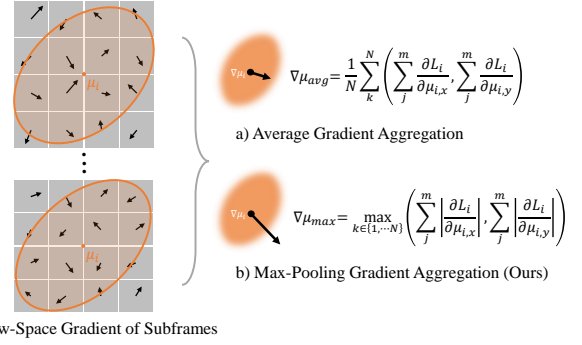
3.2.2 Global Rigid Transformation. After the first stage of optimization, we obtain an approximately accurate camera pose corresponding to the midpoint of exposure time for each training image (referred to as BAD-GS [47]). We then fix these poses for further optimization. Based on Eq. 7, we continue the derivation using:

$$\frac{\partial \mu'}{\partial T} = \frac{\partial(KT\mu)}{\partial Td}, \quad (8)$$

where K represents the camera intrinsics matrix and d is the z -axis coordinate of the projection μ . Building upon the original camera pose, we introduce an additional global transformation matrix $M_{\text{trans}} \in SE(3)$ to control the global rigid transformation of the Gaussian points in the world coordinate.

Finally, our bi-stage training mechanism is summarized as:

$$\underbrace{K(T)\mu}_{\text{Stage I}} \xrightarrow{\text{freeze } T} \underbrace{KT(M_{\text{trans}})\mu}_{\text{Stage II}}. \quad (9)$$



View-Space Gradient of Subframes

Figure 2: Subframe Gradient Aggregation via Max-Pooling.

Stage I (Camera Pose Refinement) only optimizes the camera poses T to achieve preliminary geometric alignment between consecutive input images. Stage II (Camera Pose Refinement) then freezes the approximately accurate camera poses and optimizes the global transformation M_{trans} to further deblur 3D scenes. Benefitting from the novel design, our method can significantly improve the accuracy and robustness of 3D reconstruction and enhance both computational efficiency and stability.

3.2.3 Subframe Gradient Aggregation via Max-Pooling. To resolve gradient conflicts induced by motion blur and multi-view discrepancies, we propose a subframe gradient aggregation strategy that prioritizes dominant optimization directions.

As shown in Fig. 2, during the bi-stage training process, for each input frame containing n subframes, these subframes collectively constitute temporal slices of motion-blurred sequences, which are utilized to synthesize virtual motion-blurred images. We compute view-space positional gradients $\{\nabla \mu_1, \nabla \mu_2, \dots, \nabla \mu_n\}$ through differentiable rendering, where $\mu = (\mu_x, \mu_y)$ denotes the 2D Gaussian centers in view-space. These gradients are stacked to form aggregated gradient $\nabla \mu_{\text{agg}}$ via magnitude-maximizing pooling:

$$\nabla \mu_{\text{agg}}(x) = \max_{i \in \{1, \dots, n\}} |\nabla \mu_i(x)| \cdot \text{sign}(\nabla \mu_{i_{\text{max}}}(x)), \quad (10)$$

where x represents spatial coordinates and i_{max} denotes the subframe index with maximum gradient magnitude at position x . This operation preserves the strongest gradient magnitude and prevents gradient cancellation while retaining directional consistency, effectively mitigating conflicting updates from different subframes.

3.3 Space-Time Coupling Densification

For 3DGS, signals of low frequency, such as smooth geometric structures, typically converge well during optimization, while signals of high frequency (e.g., details) often exhibit gradient oscillations. However, current 3DGS-based deblurring methods overlook important spatial variations among Gaussian primitives and progressive changes in blur levels throughout different training stages. These approaches only employ a fixed densification threshold for Gaussian splitting and cloning operations, resulting in unstable camera pose optimization due to their inability to adapt to the evolving reconstruction requirements.

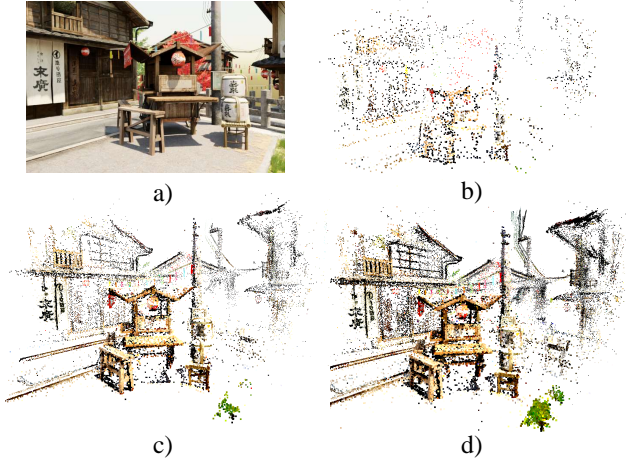


Figure 3: Visualization of Space-Time Coupling Densification effects. a) The sharp 2D image to be reconstructed; b) The initialized point cloud; c) The point cloud obtained after applying the time-aware threshold τ_t and the space-aware threshold τ_s in Stage I, with the general scene outline and low-frequency foreground been roughly reconstructed; d) The final result after applying τ_t and τ_s in Stage II. The results demonstrate that Space-Time Coupling Densification can effectively control erroneous Gaussian primitives densification caused by motion blur and improve the reconstruction performance of detail information.

To address these issues, we propose Space-Time Coupling Densification, a bi-stage dynamic coupling method designed to adaptively adjust the Gaussian densification threshold during training. In space level, because camera-motion blur tends to affect near-field Gaussian distributions with smaller depth and leads to unstable position estimation, we specially increase the densification threshold of these primitives to delay splitting. In contrast, Gaussian primitives with larger depth are not susceptible to camera-motion blur, we therefore lower their threshold to promote detail recovery. In addition, different splitting times also affect the reconstruction performance. With blurred images and inaccurate initial point cloud as input, premature splitting is prone to introduce errors. To alleviate the problem, we choose to increase the densification threshold when refining the camera pose in Stage I. Once the camera pose is optimized, we lower the threshold when applying the global rigid transformation in Stage II to facilitate splitting and restore more high-quality details.

Finally, we formulate the space-aware threshold τ_s and the time-aware threshold τ_t as:

$$\tau_s = \tau_0 \cdot (1 + \alpha \cdot e^{-\beta d}), \quad (11)$$

$$\tau_t(t) = \begin{cases} \tau_0 \cdot (1 - \gamma t) & t \in \text{Stage I} \\ \tau_0 \cdot \eta^{t-t_{split}} & t \in \text{Stage II}, \end{cases} \quad (12)$$

where τ_0 denotes the initial threshold, α controls the near-field gain, and β regulates the depth decay rate. The space-aware threshold

τ_s of near-field Gaussian primitives is significantly increased to suppress premature splitting, while τ_s of far-field primitives approaches the base value to promote detail recovery. The time-aware threshold $\tau_t(t)$ evolves throughout the whole training process, with t denoting the current training step and t_{split} marking the transition between stages. During Stage I, $\tau_t(t)$ undergoes linear decay modulated by γ , preventing excessive suppression. In Stage II, an exponential decay controlled by η enables precise regulation of high-frequency components during Global Rigid Transformation.

Our final bi-stage dynamic densification threshold $\hat{\tau}$ is determined by combining the above two thresholds as:

$$\hat{\tau} = \tau_s \cdot \tau_t(t) \quad (13)$$

As shown in Fig. 3, this joint optimization strategy effectively prevents the premature wrong generation of noisy Gaussians in blurred regions, leading to more high-quality reconstruction.

4 EXPERIMENTS

4.1 Dataset

We evaluate the performance of our method on real-world benchmark datasets, including Real-motion-blur [21] and ExBluRF [14], as well as a synthetic benchmark dataset derived from ExBluRF. The ExBluRF synthetic dataset, originally synthesized from DeblurNeRF [21], was created using Blender [4] by averaging sharp virtual images captured during the exposure time, under the assumption of consistent camera motion velocity. The resolution for the multi-view images of ExBlur dataset is 800×540 . Each scene in this dataset consists of 20 to 40 blurry images paired with corresponding sharp images. For the real-world benchmark datasets, the camera poses and sparse point clouds are obtained through Structure-from-Motion (SfM) using COLMAP [34], with a set of training and testing images. Both the real-world and synthetic ExBluRF datasets present more challenging motion-blurred images, generated with randomly varying 6-DOF camera motion trajectories, and they contain more severe motion blur compared to the Real-motion-blur dataset. The public release of ExBluRF provides accurate camera poses and initial point clouds from the corresponding sharp image pairs using COLMAP. To validate the robustness of our method on real dataset, we perform COLMAP only on the blurry images in our experiments. This process results in inaccurate camera poses and sparse point clouds due to severe blurring, which are then used to initialize the 3DGS in subsequent experiments.

4.2 Implementation Details

We implemented our method based on the official implementation of the 3D-GS framework [10] using PyTorch [28]. The Gaussian scene parameters, camera pose parameters, and global transformation parameters are optimized using the Adam optimizer, with the learning rates for both the camera pose and global transformation optimizers exponentially decaying from 1×10^{-3} to 1×10^{-5} . We set the number of virtual camera poses (i.e., n in Eq. 2) in Stage I and the number of subframes in Stage II to 21 to balance performance and computational cost. For the synthetic dataset from ExBluRF [21], we employ linear interpolation in both stages. For the Real-motion-blur dataset [21] and the real-world scenes from ExBluRF [14], different interpolation methods are adopted depending on

Table 1: Quantitative comparisons for deblurring on the real-world dataset of ExBluRF.

	Bench			Camellia			Jars			Jars2			Sunflowers		
	PSNR↑	SSIM↑	LPIPS↓												
NeRF	20.12	0.475	0.663	19.71	0.563	0.632	20.38	0.674	0.441	19.53	0.578	0.470	20.15	0.576	0.547
3DGS	19.50	0.635	0.552	20.34	0.471	0.635	21.12	0.574	0.541	20.43	0.598	0.640	17.78	0.583	0.647
Deblur-NeRF	26.15	0.721	0.241	27.33	0.713	0.319	27.12	0.703	0.235	26.64	0.729	0.298	30.10	0.814	0.172
BAD-NeRF	24.93	0.642	0.363	25.19	0.644	0.298	27.95	0.741	0.257	25.56	0.721	0.267	27.69	0.670	0.213
ExbluRF	27.44	0.732	0.215	24.79	0.702	0.237	25.16	0.678	0.214	26.63	0.698	0.319	27.62	0.805	0.232
Deblur-GS	25.35	0.684	0.227	28.78	0.791	0.282	26.96	0.752	0.227	29.56	0.786	0.129	30.22	0.785	0.167
BAD-GS	27.27	0.676	0.132	26.27	0.668	0.214	28.19	0.735	0.194	26.78	0.737	0.172	28.11	0.771	0.188
Ours	29.16	0.791	0.127	29.04	0.821	0.175	31.27	0.859	0.128	30.61	0.816	0.129	33.21	0.893	0.154

Table 2: Quantitative comparisons for deblurring on the synthetic dataset.

	Cozyroom			Factory			Pool			Tanabata			Trolley		
	PSNR↑	SSIM↑	LPIPS↓												
NeRF	23.13	0.652	0.255	22.71	0.546	0.469	27.12	0.742	0.275	20.53	0.477	0.403	21.55	0.764	0.472
3DGS	24.50	0.630	0.285	21.29	0.557	0.412	28.62	0.768	0.253	19.37	0.450	0.395	20.73	0.624	0.388
Deblur-NeRF	29.61	0.871	0.133	25.53	0.775	0.267	30.92	0.843	0.135	23.58	0.729	0.298	26.34	0.814	0.177
BAD-NeRF	30.77	0.876	0.092	28.69	0.832	0.183	32.39	0.840	0.117	25.33	0.804	0.175	26.79	0.841	0.085
ExbluRF	28.56	0.891	0.142	26.92	0.814	0.231	27.30	0.782	0.243	26.62	0.855	0.220	24.63	0.762	0.232
Deblur-GS	31.77	0.902	0.087	25.38	0.769	0.154	31.96	0.872	0.121	26.79	0.851	0.139	27.93	0.841	0.092
BAD-GS	29.16	0.883	0.096	30.88	0.864	0.104	33.22	0.918	0.071	25.11	0.735	0.150	29.68	0.897	0.078
Ours	32.13	0.915	0.076	31.35	0.904	0.097	34.47	0.895	0.098	31.12	0.874	0.112	33.18	0.924	0.081

Table 3: Quantitative comparisons for novel view synthesis.

	Real Motion Blur			Synthetic Motion Blur			Real-World Scene (ExBluRF)		
	PSNR↑	SSIM↑	LPIPS↓	PSNR↑	SSIM↑	LPIPS↓	PSNR↑	SSIM↑	LPIPS↓
NeRF	20.32	0.655	0.301	20.12	0.540	0.482	21.76	0.592	0.563
3DGS	20.46	0.641	0.428	21.44	0.612	0.477	21.39	0.591	0.632
Deblur-NeRF	26.57	0.744	0.179	23.88	0.754	0.288	28.87	0.709	0.402
BAD-NeRF	25.26	0.745	0.215	28.32	0.823	0.382	25.31	0.647	0.376
ExBluRF	23.41	0.675	0.219	27.81	0.834	0.232	26.94	0.659	0.472
Deblur-GS	25.78	0.812	0.186	28.23	0.852	0.087	30.11	0.768	0.192
BAD-GS	26.93	0.835	0.098	29.33	0.857	0.092	29.47	0.718	0.238
Ours	27.04	0.874	0.122	30.24	0.898	0.103	31.27	0.817	0.113

the specific scene characteristics. Initial estimates for the camera poses and Gaussian primitives are obtained using COLMAP [34]. All experiments were conducted on an NVIDIA RTX 3090 GPU.

4.3 Experimental Results

In our two-stage training framework, we first obtain a rough camera pose estimation by selecting the midpoint of the camera trajectory during the exposure period in Stage I. This optimized pose remains fixed throughout Stage II. To evaluate the effectiveness of our method, we select intermediate subframes from the sequence of high-quality sharp renderings generated through global rigid transformations, which are then aligned with the corresponding ground-truth images for quantitative and qualitative evaluation. Specifically, we compare our BSGS with several related methods, including 3DGS [10], Deblur-NeRF [21], BAD-NeRF [39], ExBluRF [14], DeblurGS [24], and BAD-GS [47]. Consistent with these approaches, we quantitatively assess the quality of our rendered image

using PSNR, SSIM, and LPIPS. All metrics are computed by the API from TorchMetrics [5].

4.3.1 Quantitative And Qualitative Evaluation Results. Tab. 1 and 2 present quantitative comparisons for image deblurring, with the best results highlighted in bold. These tables demonstrate the comparative performance on both real-world datasets from ExBluRF and synthetic datasets from ExBluRF. It should be noted that the results of DeblurGS and BAD-GS were obtained using their officially released codes. Since the real-world datasets from ExBluRF contain severe motion blur, significant variations are observed in the experimental results.

Tab. 3 provides quantitative comparisons for novel view synthesis on the Real-motion-blur datasets from Deblur-NeRF, as well as real-world and synthetic datasets from ExBluRF. Due to the absence of corresponding sharp ground truth images in the Real-motion-blur dataset, we only conduct novel view synthesis experiments.

Table 4: Comparison of primitive numbers for deblurring on the real and synthetic datasets of ExBluRF.

	Camellia	Sunflowers	Tanabata	Trolley
Deblur-GS	132406	154852	153094	164120
BAD-GS	225213	339439	539498	496786
Ours	13446	40210	86442	100584

Table 5: Comparison of different subframe gradient aggregation methods for deblurring on the real and synthetic dataset of ExBluRF.

Method	Stone_Lantern			Tanabata		
	PSNR \uparrow	SSIM \uparrow	LPIPS \downarrow	PSNR \uparrow	SSIM \uparrow	LPIPS \downarrow
Average	28.50	0.769	0.181	30.04	0.819	0.152
Top-K (k=5)	29.83	0.804	0.179	29.33	0.836	0.147
Max-Pooling	30.98	0.821	0.165	31.12	0.874	0.112

Compared with other 3DGS-based methods, our approach achieves superior performance in both deblurring and novel view synthesis.

Fig. 4 presents the qualitative comparisons between our method and other approaches. We selected four scenes from the ExBluRF dataset for evaluation, with camera poses of blurry input images initialized by COLMAP. Since BAD-NeRF relies on the linear trajectory to model camera motion, the method fails to restore sharp radiance fields when dealing with more severe hand-shake camera motion blur in real-world scenes. Experimental results demonstrate that our method is capable of reconstructing significantly sharper scenes. Further visualization results can be found in our supplementary materials.

To further evaluate our method, we specially compute the error maps, as shown in Fig. 5. The error map is generated by computing the difference between the captured blurry image and the corresponding virtual image synthesized during the training process. The results show that our approach targets the finer details.

To evaluate the efficiency of our method in terms of computational performance and memory usage in 3D scene representation, we compare the Gaussian primitive numbers of different methods, as shown in Tab. 4. The results show that our method significantly reduces the number of points while maintaining competitive deblurring performance. This reduction not only lowers memory consumption but also accelerates rendering and optimization processes, making our method more practical for real-world applications.

In Tab. 5, we compare the performance of different subframe gradient aggregation methods on the real and synthetic dataset of ExBluRF. "Average" represents the mean aggregation of all subframe gradients, whereas "Top-K" (where we set k=5 in our experiments) computes the average over the k largest gradients from the subframes. The results indicate that our max-pooling aggregation strategy shows superior performance across all evaluation metrics. This approach effectively preserves the most critical gradient features while robustly addressing gradient inconsistencies among subframes, thereby enabling more stable optimization and enhanced reconstruction quality for motion-blurred scenes.

Table 6: Ablation studies on each element of our proposed method for deblurring on the real and synthetic dataset.

Method			Camellia			Tanabata		
Stage I	Stage II	STDC	PSNR \uparrow	SSIM \uparrow	LPIPS \downarrow	PSNR \uparrow	SSIM \uparrow	LPIPS \downarrow
✓			26.59	0.712	0.225	28.39	0.683	0.276
	✓		27.17	0.734	0.197	28.72	0.719	0.210
✓		✓	27.44	0.760	0.181	29.15	0.794	0.225
	✓	✓	28.58	0.805	0.179	30.12	0.827	0.127
✓		✓	27.70	0.751	0.183	28.94	0.725	0.169
✓	✓	✓	29.04	0.821	0.175	31.12	0.874	0.112

4.3.2 Ablation Studies. We further evaluate the effectiveness of the two-stage approach and Space-Time Coupling Densification. As shown in Tab. 6, each component is fundamental for reconstructing sharp scenes, with the highest performance being achieved when all elements are integrated cohesively. Space-Time Coupling Densification contributes positively in both training stages.

Fig. 6 compares the quality of reconstruction between using a constant threshold for Gaussian densification and those proposed in Space-Time Coupling Densification. It is clear that the rendering quality of the foreground remains comparable in both strategies. However, our proposed Space-Time Coupling Densification strategy reconstructs more high-quality distant background regions, thus leading to a more detailed and coherent overall scene.

5 Conclusion

In this paper, we introduce a novel approach for camera motion deblurring in 3D Gaussian scene representation. Our approach employs a two-stage training trajectory to reconstruct sharper scenes with motion-blurred images. The first stage roughly optimizes the camera pose. Then, with the fixed camera pose, the second stage applies global rigid transformations to the Gaussian primitives, simulating the process of camera motion blur generation. Additionally, we introduce Space-Time Coupling Densification strategy to adaptively adjust the densification threshold, improving scene reconstruction quality. Experimental results demonstrate that our method outperforms all existing deblurring approaches, producing high-quality and robust scene representations.

Acknowledgments

This work was supported by the National Natural Science Foundation of China (No. T2322012, No. 62172218).

References

- [1] Anpei Chen, Zexiang Xu, Andreas Geiger, Jingyi Yu, and Hao Su. 2022. Tensor4: Tensorial radiance fields. In *European conference on computer vision*. 333–350.
- [2] Wenbo Chen and Ligang Liu. 2024. Deblur-GS: 3D Gaussian Splatting from Camera Motion Blurred Images. *ACM on Computer Graphics and Interactive Techniques* 7, 1 (2024), 1–15.
- [3] Jaeyoung Chung, Suyoung Lee, Hyeongjin Nam, Jaerin Lee, and Kyoung Mu Lee. 2023. LucidDreamer: Domain-free Generation of 3D Gaussian Splatting Scenes. *arXiv preprint arXiv:2311.13384* (2023).
- [4] Blender Online Community. 2018. *Blender - a 3D modelling and rendering package*. Blender Foundation.
- [5] Nicki Skaftø Detlefsen, Jiri Borovec, Justus Schock, Ananya Harsh, Teddy Koker, Luca Di Liello, Daniel Stancl, Changsheng Quan, Maxim Grechkin, and William Falcon. 2022. *TorchMetrics - Measuring Reproducibility in PyTorch*.
- [6] Sara Fridovich-Keil, Alex Yu, Matthew Tancik, Qinhong Chen, Benjamin Recht, and Angjoo Kanazawa. 2022. Plenoxels: Radiance fields without neural networks. In *IEEE/CVF conference on computer vision and pattern recognition*. 5501–5510.

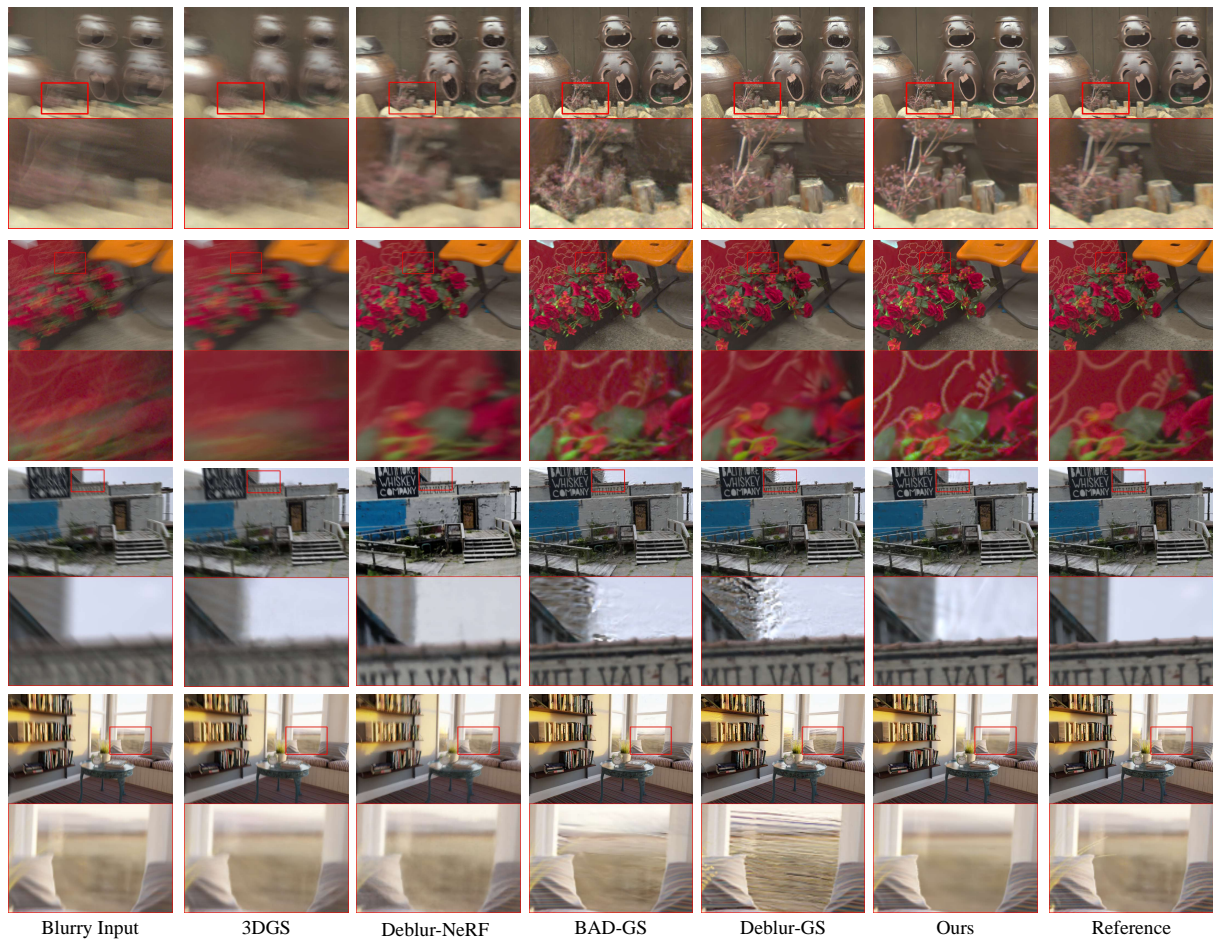


Figure 4: Qualitative comparison for deblurring on the synthetic and real-world scenes. The first two rows are from synthetic datasets while the last two rows are from real-world datasets. The results demonstrate our method’s superior deblurring and detail restoration performance compared to prior approaches.

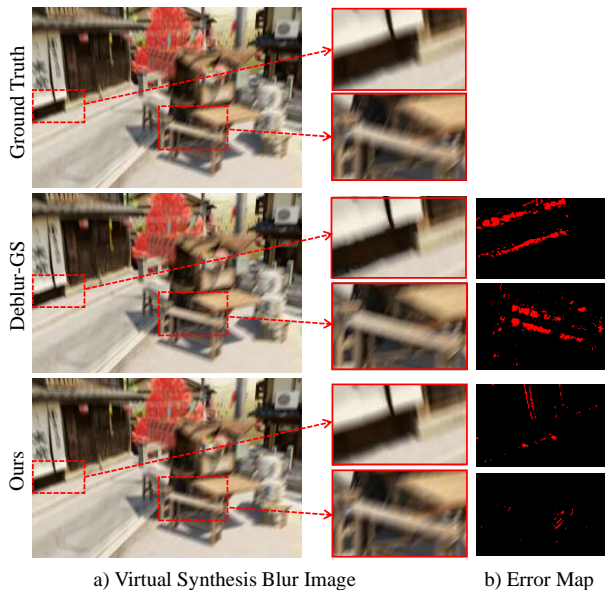


Figure 5: Visual comparison with error maps in Trolley scene.

- [7] Guy Gafni, Justus Thies, Michael Zollhofer, and Matthias Nießner. 2021. Dynamic neural radiance fields for monocular 4d facial avatar reconstruction. In *IEEE/CVF Conference on Computer Vision and Pattern Recognition*. 8649–8658.
- [8] Hongyun Gao, Xin Tao, Xiaoyong Shen, and Jiaya Jia. 2019. Dynamic scene deblurring with parameter selective sharing and nested skip connections. In *IEEE/CVF conference on computer vision and pattern recognition*. 3848–3856.
- [9] Wei Jiang, Kwang Moo Yi, Golnoosh Samei, Oncel Tuzel, and Anurag Ranjan. 2022. Neuman: Neural human radiance field from a single video. In *European Conference on Computer Vision*. 402–418.
- [10] Bernhard Kerbl, Georgios Kopanas, Thomas Leimkühler, and George Drettakis. 2023. 3D Gaussian Splatting for Real-Time Radiance Field Rendering. *ACM Transactions on Graphics* 42, 4 (2023).
- [11] Orest Kupyn, Tetiana Martyniuk, Junru Wu, and Zhangyang Wang. 2019. Deblurgan-v2: Deblurring (orders-of-magnitude) faster and better. In *IEEE/CVF international conference on computer vision*. 8878–8887.
- [12] Byeonghyeon Lee, Howoong Lee, Xiangyu Sun, Usman Ali, and Eunbyung Park. 2024. Deblurring 3d gaussian splatting. In *European Conference on Computer Vision*. 127–143.
- [13] Dogyoon Lee, Minhyeok Lee, Chajin Shin, and Sangyoun Lee. 2023. Dp-nerf: Deblurred neural radiance field with physical scene priors. In *IEEE/CVF Conference*

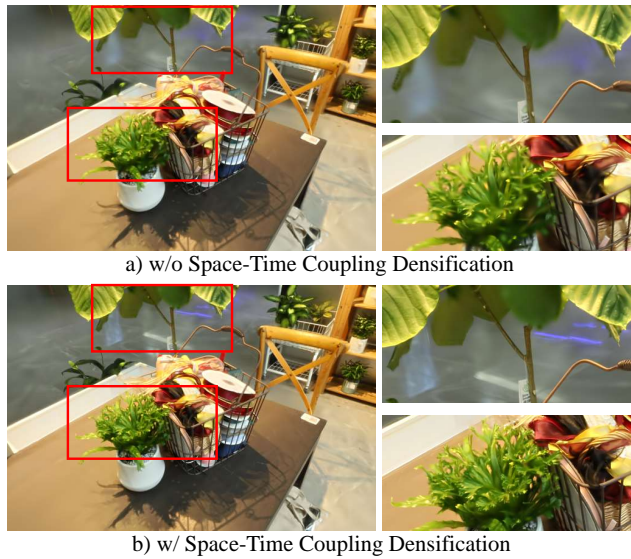


Figure 6: Ablation studies on Space-Time Coupling Densification.

- on *Computer Vision and Pattern Recognition*. 12386–12396.
- [14] Dongwoo Lee, Jeongtaek Oh, Jaesung Rim, Sunghyun Cho, and Kyoung Mu Lee. 2023. Exblurf: Efficient radiance fields for extreme motion blurred images. In *IEEE/CVF International Conference on Computer Vision*. 17639–17648.
- [15] Junghe Lee, Donghyeong Kim, Dogyoon Lee, Suhwan Cho, and Sangyoun Lee. 2024. Crim-gs: Continuous rigid motion-aware gaussian splatting from motion blur images. *arXiv preprint arXiv:2407.03923* (2024).
- [16] Jungho Lee, Dogyoon Lee, Minhyeok Lee, Donghyung Kim, and Sangyoun Lee. 2024. Smurf: Continuous dynamics for motion-deblurring radiance fields. *arXiv preprint arXiv:2403.07547* (2024).
- [17] Tianye Li, Mira Slavcheva, Michael Zollhofer, Simon Green, Christoph Lassner, Changil Kim, Tanner Schmidt, Steven Lovegrove, Michael Goesele, Richard Newcombe, et al. 2022. Neural 3d video synthesis from multi-view video. In *IEEE/CVF conference on computer vision and pattern recognition*. 5521–5531.
- [18] Zhengqi Li, Simon Niklaus, Noah Snavely, and Oliver Wang. 2021. Neural scene flow fields for space-time view synthesis of dynamic scenes. In *IEEE/CVF Conference on Computer Vision and Pattern Recognition*. 6498–6508.
- [19] Yixun Liang, Xin Yang, Jiantao Lin, Haodong Li, Xiaogang Xu, and Yingcong Chen. 2023. Luciddreamer: Towards high-fidelity text-to-3d generation via interval score matching. *arXiv preprint arXiv:2311.11284* (2023).
- [20] Huan Ling, Seung Wook Kim, Antonio Torralba, Sanja Fidler, and Karsten Kreis. 2024. Align Your Gaussians: Text-to-4D with Dynamic 3D Gaussians and Composed Diffusion Models. In *IEEE Conference on Computer Vision and Pattern Recognition*.
- [21] Li Ma, Xiaoyu Li, Jing Liao, Qi Zhang, Xuan Wang, Jue Wang, and Pedro V Sander. 2022. Deblur-nerf: Neural radiance fields from blurry images. In *IEEE/CVF Conference on Computer Vision and Pattern Recognition*. 12861–12870.
- [22] Ben Mildenhall, Pratul P Srinivasan, Matthew Tancik, Jonathan T Barron, Ravi Ramamoorthi, and Ren Ng. 2021. Nerf: Representing scenes as neural radiance fields for view synthesis. *Commun. ACM* 65, 1 (2021), 99–106.
- [23] Seungjun Nah, Tae Hyun Kim, and Kyoung Mu Lee. 2017. Deep multi-scale convolutional neural network for dynamic scene deblurring. In *IEEE conference on computer vision and pattern recognition*. 3883–3891.
- [24] Jeongtaek Oh, Jaeyoung Chung, Dongwoo Lee, and Kyoung Mu Lee. 2024. DeblurGS: Gaussian Splatting for Camera Motion Blur. *arXiv preprint arXiv:2404.11358* (2024).
- [25] Hao Ouyang, Tiancheng Sun, Stephen Lombardi, and Kathryn Heal. 2023. Text2Immersion: Generative Immersive Scene with 3D Gaussians. *Arxiv* (2023).
- [26] Keunhong Park, Utkarsh Sinha, Jonathan T Barron, Sofien Bouaziz, Dan B Goldman, Steven M Seitz, and Ricardo Martin-Brualla. 2021. Nerfies: Deformable neural radiance fields. In *IEEE/CVF international conference on computer vision*. 5865–5874.
- [27] Keunhong Park, Utkarsh Sinha, Peter Hedman, Jonathan T Barron, Sofien Bouaziz, Dan B Goldman, Ricardo Martin-Brualla, and Steven M Seitz. 2021. Hypernerf: A higher-dimensional representation for topologically varying neural radiance fields. *arXiv preprint arXiv:2106.13228* (2021).
- [28] Adam Paszke, Sam Gross, Francisco Massa, Adam Lerer, James Bradbury, Gregory Chanan, Trevor Killeen, Zeming Lin, Natalia Gimelshein, Luca Antiga, et al. 2019. Pytorch: An imperative style, high-performance deep learning library. *Advances in neural information processing systems* 32 (2019).
- [29] Cheng Peng and Rama Chellappa. 2022. Pdrf: Progressively deblurring radiance field for fast and robust scene reconstruction from blurry images. *arXiv preprint arXiv:2208.08049* (2022).
- [30] Cheng Peng, Yutao Tang, Yifan Zhou, Nengyu Wang, Xijun Liu, Deming Li, and Rama Chellappa. 2024. Bags: Blur agnostic gaussian splatting through multi-scale kernel modeling. In *European Conference on Computer Vision*. 293–310.
- [31] Sida Peng, Junting Dong, Qianqian Wang, Shangzhan Zhang, Qing Shuai, Xiaowei Zhou, and Hujun Bao. 2021. Animatable neural radiance fields for modeling dynamic human bodies. In *IEEE/CVF International Conference on Computer Vision*. 14314–14323.
- [32] Albert Pumarola, Enric Corona, Gerard Pons-Moll, and Francesc Moreno-Noguer. 2021. D-nerf: Neural radiance fields for dynamic scenes. In *IEEE/CVF conference on computer vision and pattern recognition*. 10318–10327.
- [33] Jiawei Ren, Liang Pan, Jiaxiang Tang, Chi Zhang, Ang Cao, Gang Zeng, and Ziwei Liu. 2023. DreamGaussian4D: Generative 4D Gaussian Splatting. *arXiv preprint arXiv:2312.17142* (2023).
- [34] Johannes L Schonberger and Jan-Michael Frahm. 2016. Structure-from-motion revisited. In *IEEE conference on computer vision and pattern recognition*. 4104–4113.
- [35] Shuochen Su, Mauricio Delbracio, Jue Wang, Guillermo Sapiro, Wolfgang Heidrich, and Oliver Wang. 2017. Deep video deblurring for hand-held cameras. In *IEEE conference on computer vision and pattern recognition*. 1279–1288.
- [36] Jiaxiang Tang, Jiawei Ren, Hang Zhou, Ziwei Liu, and Gang Zeng. 2023. DreamGaussian: Generative Gaussian Splatting for Efficient 3D Content Creation. *arXiv preprint arXiv:2309.16653* (2023).
- [37] Xin Tao, Hongyun Gao, Xiaoyong Shen, Jue Wang, and Jiaya Jia. 2018. Scale-recurrent network for deep image deblurring. In *IEEE conference on computer vision and pattern recognition*. 8174–8182.
- [38] Edgar Tretschk, Ayush Tewari, Vladislav Golyanik, Michael Zollhofer, Christoph Lassner, and Christian Theobalt. 2021. Non-rigid neural radiance fields: Reconstruction and novel view synthesis of a dynamic scene from monocular video. In *IEEE/CVF International Conference on Computer Vision*. 12959–12970.
- [39] Peng Wang, Lingzhe Zhao, Ruijie Ma, and Peidong Liu. 2023. BAD-Nerf: Bundle Adjusted Deblur Neural Radiance Fields. In *IEEE/CVF Conference on Computer Vision and Pattern Recognition*. 4170–4179.
- [40] Chung-Yi Weng, Brian Curless, Pratul P Srinivasan, Jonathan T Barron, and Ira Kemelmacher-Shlizerman. 2022. Humannerf: Free-viewpoint rendering of moving people from monocular video. In *IEEE/CVF conference on computer vision and pattern recognition*. 16210–16220.
- [41] Dejia Xu, Hanwen Liang, Neel P Bhatt, Hezhen Hu, Hanxue Liang, Konstantinos N Plataniotis, and Zhangyang Wang. 2024. Comp4D: LLM-Guided Compositional 4D Scene Generation. *arXiv preprint arXiv:2403.16993* (2024).
- [42] Chi Yan, Delin Qu, Dan Xu, Bin Zhao, Zhiqiang Wang, Dong Wang, and Xuelong Li. 2024. Gs-slam: Dense visual slam with 3d gaussian splatting. In *IEEE/CVF Conference on Computer Vision and Pattern Recognition*. 19595–19604.
- [43] Taoran Yi, Jiemin Fang, Junjie Wang, Guanjun Wu, Lingxi Xie, Xiaopeng Zhang, Wenyu Liu, Qi Tian, and Xinggang Wang. 2024. GaussianDreamer: Fast Generation from Text to 3D Gaussians by Bridging 2D and 3D Diffusion Models. In *CVPR*.
- [44] Yuyang Yin, Dejia Xu, Zhangyang Wang, Yao Zhao, and Yunchao Wei. 2023. 4dgen: Grounded 4d content generation with spatial-temporal consistency. *arXiv preprint arXiv:2312.17225* (2023).
- [45] Alex Yu, Ruilong Li, Matthew Tancik, Hao Li, Ren Ng, and Angjoo Kanazawa. 2021. Plenotrees for real-time rendering of neural radiance fields. In *IEEE/CVF international conference on computer vision*. 5752–5761.
- [46] Syed Waqas Zamir, Aditya Arora, Salman Khan, Munawar Hayat, Fahad Shahbaz Khan, Ming-Hsuan Yang, and Ling Shao. 2021. Multi-stage progressive image restoration. In *IEEE/CVF conference on computer vision and pattern recognition*. 14821–14831.
- [47] Lingzhe Zhao, Peng Wang, and Peidong Liu. 2024. Bad-gaussians: Bundle adjusted deblur gaussian splatting. In *European Conference on Computer Vision*.
- [48] Xiaoyu Zhou, Xingjian Ran, Yajiao Xiong, Jinlin He, Zhiwei Lin, Yongtao Wang, Deqing Sun, and Ming-Hsuan Yang. 2024. Gala3d: Towards text-to-3d complex scene generation via layout-guided generative gaussian splatting. *arXiv preprint arXiv:2402.07207* (2024).